Size dependence of static polymer droplet behavior from many-body dissipative particle dynamics simulation

Naoki Kadoya and Noriyoshi Arai*
Kindai University, 3-4-1 Kowakae, Higashiosaka, Osaka, 577-8502 Japan
(Received 4 August 2016; revised manuscript received 6 February 2017; published 24 April 2017)

We used molecular simulation to study the static behavior of polymer droplets in vacuum and on solid surfaces, namely the size of the droplet and the contact angle, respectively. The effects of the polymer chain length and the total number of particles were calculated by the many-body dissipative particle dynamics method. For the spherical droplet containing the same number of particles, we show that its radius depends on the polymer chain length. The radius of the droplet is also proportional to one-third power of the total number of particles for all given chain lengths. For the hemispherical droplet, the contact angle increases with the number of particles in the droplet, and this effect is relatively strong, especially for longer polymer chains. The effect of wettability of the solid surface was also investigated by using polymerphobic (low-affinity) and polymerphilic (high-affinity) surfaces. As the chain length increases, the contact angle on the low-affinity surface decreases, while that on the hydrophilic surface increases. The simulation reveals that there is a critical affinity for the monomer on the solid surface; above and below which the wettability increases and decreases as the molecular length increases, respectively.

DOI: 10.1103/PhysRevE.95.043109

I. INTRODUCTION

Microdroplet technology has been employed in applications via microfluidic functionality in many fields, including chemistry, biology, and engineering [1]. In particular, the control of wetting behavior on a solid surface is a very important research topic that spans physics and engineering. It is well known that microtextured or nanotextured hydrophobic surfaces can become superhydrophobic [2]. Many plants and insects in the natural world have used such superhydrophobic structures effectively [3–6]. For example, a water strider could "walk" on the water surface owing to its distinctive legs. The surface of a lotus leaf shows strong hydrophobic property due to the microscale bumps, thereby preventing dirt from adhering to the leaf. Moreover, the microstructure of the spider silk increases its ability to collect water. The interest to mimic such natural structures is growing in the field of engineering, and the study of microdroplets and wettability has attracted attention in recent years.

Polymer droplets are especially useful in microdroplet technology. Inkjet printing has emerged as an attractive patterning technique for functional polymers. Because the formed microdroplets enable high-resolution definition of channel lengths in several micrometers, it has been used in organic electroluminescence display devices and organic transistors [7]. In regenerative medical engineering, the inkjet technique is a promising biofabrication tool for artificial cells and bones through the mapping of biological polymers [8,9].

Hence, inkjet printing using polymer droplets has been studied extensively as an important next-generation technology [10–12]. For example, Wang *et al.* [10] evaluated the influence of solution viscosity, ink volume, and contact angle in the process of dewetting of inkjet-printed droplets of a conducting polymer. They found that dewetting is determined by the competition between reduced liquid thickness and increased liquid viscosity caused by water evaporation. Independently, Léonforte and Müller [11] investigated the static and dynamic properties of a polymer brush-liquid system. They also studied the wetting behavior of polymer droplets with different contact angles and on substrates that differ in softness. They found that the surface and droplet compliance can be tuned independently to the surface softness, and a wide range of wetting and deformation behaviors can be induced by varying the droplet size. Perelaer *et al.* [12] experimentally studied the spreading of inkjet-printed droplets of a polystyrene and toluene solution on solid dry surfaces. They showed that the in-flight evaporation of the solvent depends on not only the vapor pressure but also the viscosity of the solution, since a more viscous solution leaves a smaller dried droplet on the substrate.

It is known that the properties of polymer melts strongly depend on the chain length of the polymer (polymerization degree) [13,14]. When the chains are sufficiently short to remain unentangled in the melt, their dynamics can be described by the Rouse model [13]. In this model, the single chain diffuses according to Brownian motion of particles connected by harmonic springs. This model can describe the concentration-dependent terminal relaxation time, terminal modulus, and diffusion coeffcient of semidilute short-chain polymer melts. For example, the scaling relationships of the diffusion constant D and the viscosity η with the chain length N are written as $D \propto N^{-1}$ and $\eta \propto N$.

On the other hand, when the molecular weight of the polymer exceeds a certain critical value, M_c, the behavior of polymer melt cannot be predicted by the Rouse model owing to chain entanglement. In such systems, the transverse motion of a polymer chain is restricted by the surrounding chains. As a result, the viscosity of the polymer melt increases dramatically. This concept leads to the reptation model [15,16]. In the reptation regime, the corresponding scaling laws obtained are $D \propto N^{-2}$ and $\eta \propto N^3$.

Therefore, the chain length is one important index used to understand the behavior of polymer melts. Haine *et al.* [17,18] studied the spreading dynamics of polymer droplets using

*arai@mech.kindai.ac.jp

molecular dynamics (MD) simulation. They found that the diffusive behavior of the precursor foot is in good agreement with the molecular kinetic model. In another study of the polymer-based lubricant droplet spreading on a solid substrate, Noble *et al.* [19] focused on the effects of the molecular mass, molecular length, and functional end groups of the lubricant and the substrate. The functional end groups of the polymer were shown to play a critical role in droplet spreading. However, various studies [17–21] have been performed over the past few decades, but those incompletely reveal the effects of the chain length and size of the polymer droplet on the equilibrium properties, such as the droplet shape and contact angle with a solid surface. Such a relationship is vital in applications such as controlling the wettability and ink-jet printing. In this paper, we performed molecular simulations for droplets of polymers with various chain lengths and total number of particles, both on the solid surface and in vacuum. The relationship between the number of particles and the radius of the droplet in vacuum was obtained. Then, we clarify the effects of the number of particles and chain length on the contact angle of a hemispherical droplet on a solid surface.

II. METHOD AND CONDITIONS

A. Many-body dissipative particle dynamics

To investigate the polymer droplet system, we employed the many-body dissipative particle dynamics (MDPD) method [22–25]. In the classical dissipative particle dynamics (DPD) method [26–28], the interaction between the particles contains only repulsive forces and reflects the mean force between two coarse-grained particles [29,30]. However, the classical DPD method fails to produce a sharp density difference in cases including the vapor-liquid interface, the bubble formation, and the capillary flow in a cylindrical tube. To overcome this limitation, Warren [24] introduced the following attractive term into the DPD:

$$\boldsymbol{F}_{ij}^{\mathrm{C}} = a_{ij}\left(1-\frac{|\boldsymbol{r}_{ij}|}{r_c}\right)\boldsymbol{n}_{ij} + b_{ij}\left(\bar{\rho}_i+\bar{\rho}_j\right)\left(1-\frac{|\boldsymbol{r}_{ij}|}{r_d}\right)\boldsymbol{n}_{ij}. \tag{1}$$

Here, $\bar{\rho}_i$ is the local density at the particle, and r_c and r_d are cutoff distances. The first term in Eq. (1) represents an attractive interaction, and the second term represents the many-body effect, which behaves as a repulsive interaction. Hence, the values of a_{ij} and b_{ij} are chosen to be negative and positive, respectively. The local density is given by

$$\bar{\rho}_i = \sum_{i\neq j}\frac{15}{2\pi r_d^3}\left(1-\frac{|\boldsymbol{r}_{ij}|}{r_d}\right)^2. \tag{2}$$

Warren [24] performed a simulation of pendant droplets with the vapor-liquid interface using the MDPD method. He reported that the shape obtained from simulation agrees with the theoretical one. MDPD method has since been employed in studies of the contact angle in capillary flow [31,32], liquid droplets on solid surfaces [33,34], and bubble formation [35], etc.

In the current MDPD simulations, we use reduced units for the cutoff radius r_c, the particle mass m, and the energy $k_{\mathrm{B}}T$, where T is the temperature and k_{B} is the Boltzmann's constant. Hence, $r_c = m = k_{\mathrm{B}}T = 1$. And the time unit is defined as $\tau = \sqrt{mr_c^2/k_{\mathrm{B}}T} = 1$.

B. Segmental repulsion potential

In the MDPD method, a soft potential is also used as the interaction between particles. Therefore, it is known to be unable to reproduce the entanglement effects [36,37]. To capture the entanglement behavior of the polymer, an improved segmental repulsion potential (mSRP) [38] was applied with the soft DPD potential in our simulation. The entanglement force ($\boldsymbol{F}_{kl}^{\mathrm{E}}$) is given by

$$\boldsymbol{F}_{kl}^{\mathrm{E}} = \begin{cases} a_{kl}^{\mathrm{E}}\left(1-\frac{|\boldsymbol{d}_{kl}|^2}{d_c}\right)\hat{\boldsymbol{d}}_{kl}, & |\boldsymbol{d}_{kl}| \leqslant d_c \\ 0, & |\boldsymbol{d}_{kl}| > d_c \end{cases}, \tag{3}$$

where k and l represent bond indexes, $\boldsymbol{F}_{kl}^{\mathrm{E}}$ is the force acting between bonds k and l separated by a distance $\boldsymbol{d}_{kl}$, a^{E} is the force constant, d_c is the cutoff radius for the entanglement force, $\boldsymbol{d}_{kl} = \boldsymbol{d}_k - \boldsymbol{d}_l$, and $\hat{\boldsymbol{d}}_{kl} = \boldsymbol{d}_{kl}/|\boldsymbol{d}_{kl}|$. The position of a bond is defined as the midpoint of the bond vector $\boldsymbol{P}_k$. Therefore, the distance between two bonds can be computed as $\boldsymbol{d}_{kl} = \boldsymbol{P}_k - \boldsymbol{P}_l$. Moreover, $\boldsymbol{F}_{kl}^{\mathrm{E}}$ is decomposed into particle forces. For particles i and j in bond k, $\boldsymbol{F}_i = 0.5\ \boldsymbol{F}_{kl}^{\mathrm{E}}$ and $\boldsymbol{F}_j = 0.5\ \boldsymbol{F}_{kl}^{\mathrm{E}}$. In our simulations, the cutoff radius d_c and the force constant a_{kl}^{E} were set at $0.9\ r_c$ and $100\ k_{\mathrm{B}}T/r_c$, respectively.

C. Simulation conditions

We prepared six systems that differ from each other in the number of particles (N), $N = 1920$, 3840, 7680, 15 360, 23 040, and 30 720. In each case, five different chain lengths (N_c) were examined: $N_c = 1$, 2, 4, 8, and 16. For example, $N_c = 1$ means monomers with a single particle and $N_c = 2$ means a dumbbell-shaped dimer molecule. Each particle and its nearest-neighbor in the molecule are connected by a harmonic spring with a spring constant of $100\ k_{\mathrm{B}}T/r_c^2$, and the equilibrium bond length is $0.86\ r_c$. These values are widely used in DPD simulations of the polymer [39–41]. The value corresponds to the first peak of the radial distribution function in the monomer solution.

Moreover, as shown in Fig. 1, two types of systems were prepared: a spherical configuration [Figs. 1(a1), 1(a2), and 1(a3)], and a hemispherical configuration on a solid surface [Figs. 1(b1), 1(b2), and 1(b3)]. The solid wall is composed of 40 000 particles on a diamond lattice with a lattice constant $\alpha = 0.5\ r_c$. Therefore, we examined 60 simulations in total.

All simulations were performed in the NVT ensemble. In the DPD simulation, the thermostat is achieved by pairwise random and dissipative forces. These forces are coupled via the fluctuation-dissipation theorem [27]. The noise amplitude (σ) and the friction coefficient (γ) are parameters included in dissipative and random forces, respectively. They satisfy the $\sigma = \sqrt{2\gamma k_{\mathrm{B}}T}$, which reproduce a canonical ensemble. Hence, σ and γ were set at 3.0 and 4.5, respectively. The temperature was set at $0.5\ k_{\mathrm{B}}T$ to substantially eliminate the effect of the thermal fluctuations. The total number of particles (N_{total}) in the droplet was 1920 to 70 720, depending on the droplet size. Particles in the polymer and the solid wall are labeled by the letters P and S, respectively. In our simulation, interaction parameters in Eq. (1) are described by $a_{\mathrm{PP}} = -40$

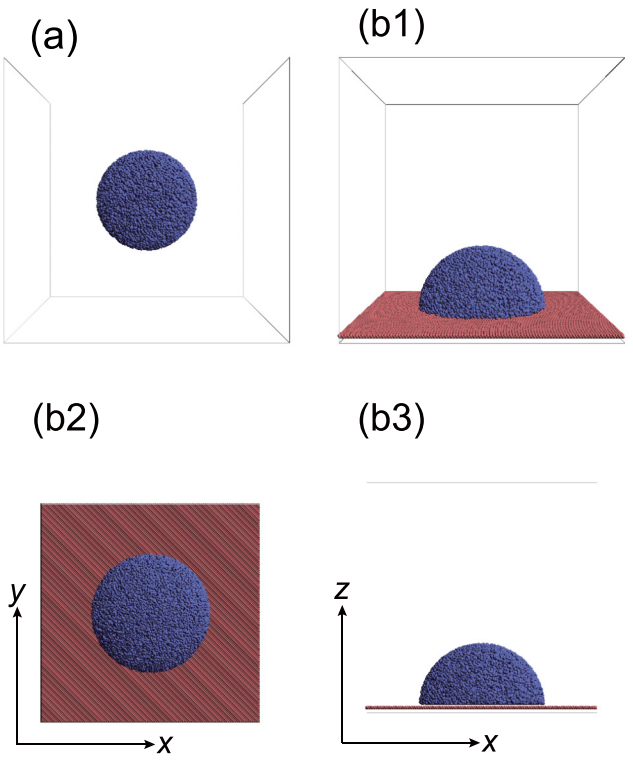

FIG. 1. Snapshots of initial configuration of droplet systems ($\tau = 0$). A spherical droplet system (a1) in the x-y plane view (a2) and in the x-z plane (a3). A hemispherical droplet on a solid surface system (b1) in the x-y plane (b2) and in the x-z plane (b3).

k_BT/r_c, $a_{PS} = -25\ k_BT/r_c$, $a_{SS} = 0\ k_BT/r_c$, and $b_{PP} = b_{PS} = b_{SS} = 25\ k_BT/r_c$, which are representative values for the solid-liquid-vapor coexisting system, such as a capillary flow with a water-oil interface [31,32] and a droplet sliding across micropillars [34]. Based on these studies, we use 0.75 r_c and 0.005 τ as the cutoff radius d_c for the repulsive conservation force and Δt, respectively. Moreover, to investigate solid walls of different wettability, when $-25\ k_BT/r_c$ is defined by the polymer-neutral surface, the interaction parameter a_{PS} was set to $-15\ k_BT/r_c$ and $-35\ k_BT/r_c$ for polymerphobic and polymerphilic surfaces, respectively. In our simulation, each run is 5000 τ in duration in order to reproduce the equilibrium droplet. The reported data are averaged over the last 500 τ of simulation.

III. RESULTS AND DISCUSSION

A. Validation of simulation method

Some early studies [24,42,43] report that MDPD method can reproduce the Laplace law. However, to satisfy the law for the system reproduced by the MDPD method with the SRP has not yet been verified. In this section, we describe the validation of current simulation method by confirming the droplet behaviors satisfy the Laplace law based on Tiwari and Abraham's study [44].

The Laplace law predicts a relationship between the pressures inside and outside of a droplet at equilibrium. The relationship is given by

$$p_{in} - p_{out} = \frac{2\sigma_s}{R}, \tag{4}$$

where p is the pressure, the subscripts "in" and "out" represent the region inside and outside of the droplet, respectively, σ_s is the surface tension, and R is the radius of the droplet.

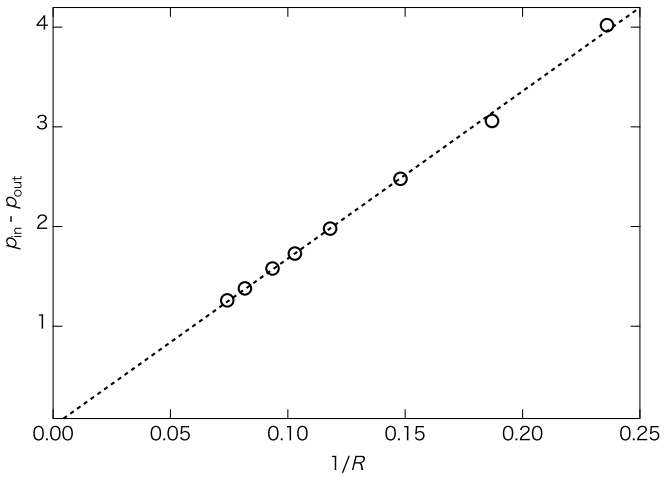

FIG. 2. Verification of Laplace law for the our MDPD model. The vertical axis is a pressure difference ($p_{in} - p_{out}$) between inside and outside of the drop, and the horizontal axis is a reciprocal of the radius (R). The dashed line is the Laplace law prediction.

To establish the relationship between the pressure difference and $1/R$, we examined eight simulations with 1920, 3840, 7680, 15 360, 23 040, 30 720, 46 080, and 61 440 particles, respectively. The pressure is calculated by the virial equation:

$$p = \rho k_B T + \frac{1}{6V} \sum_i \sum_j \boldsymbol{r}_{ij} \cdot \boldsymbol{F}^C_{ij}. \tag{5}$$

Here, ρ and V are the density and the volume of droplet, respectively. We chose the virial radius r to calculate the pressure inside of the liquid droplet. This is 0.7 times as large as the equilibrium radius R of the droplet. This procedure can avoid the pressure fluctuations near the interface [44].

The simulation results obtained are shown in Fig. 2. The pressure was computed based on averaging the instantaneous values over 50 000 time steps. The pressure difference increased in proportion to $1/R$. The data were fitted to the linear function [Eq. (4)]; the surface tension σ_s was 0.50 k_BT/r_c^2. The simulation method satisfies the Laplace law; therefore, the validity of the simulation method is proved.

B. Droplet radius

In the first series of simulations, we set the DPD particles to form a spherical shape as shown in Fig. 1(a) and then computed the radius of the polymer droplet to investigate the effects of the chain length and system size on the radius of the droplet. First, we calculated the density distribution by considering the concentric spherical shells around the center of mass of the droplet. Then, the density distribution is drawn by computing the density of each shell. Here the distance between adjacent

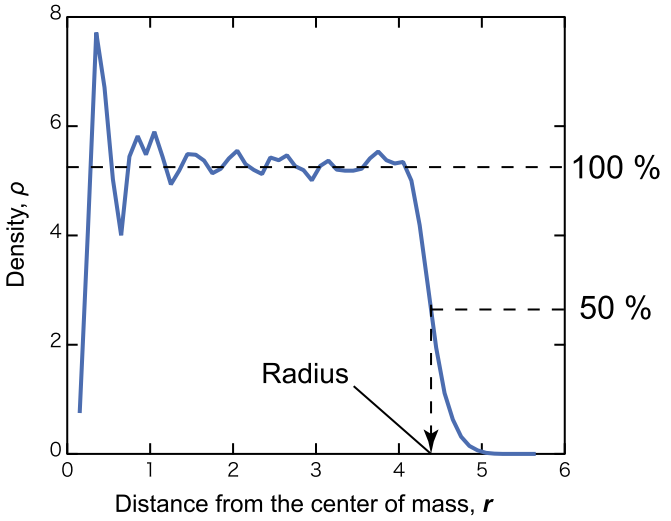

FIG. 3. An outline of the computational procedure of the droplet radius. To calculate the density distribution, the concentric spherical shells around the center of mass of the droplet is considered. Here the distance between adjacent shells (dr) is set to 0.1. The density distribution at $N = 1920$ and $N_c = 1$. We defined R as the radius when ρ drops to half the value near the center of mass.

shells, dr, is set to 0.1. Figure 3 shows the density distribution at $N = 1920$ and $N_c = 1$. The vertical axis is the density (ρ), and the horizontal axis is the distance, r, from the center of mass of the droplet. The value of ρ is almost constant ($\sim$5.2) for $r < 4.0$. When r becomes greater than 4.0, the density decreases drastically. We defined R as the radius when ρ drops to half the value near the center of mass ($\sim$2.6 in this case). For $N = 1920$ and $N_c = 1$, R is approximately 4.2.

We summarized the computation results in Fig. 4(a) by plotting R against the number of particles N. As N increases, R increases with N_c, as expected. The solid lines are the fitting results using the following equation:

$$R(N) = C \times N^{1/3}. \tag{6}$$

Here, C is a constant. The value of 1/3 is chosen because the volume of a spherical droplet is $\frac{4}{3}\pi R^3$. Therefore, independent of the polymer chain length, the radius of the droplet is proportional to $N^{1/3}$. Since the effect of the system size (N) on the droplet radius is very weak, it is possible to predict the shape and size of a polymer droplet by simulating a smaller system.

We computed the surface tension σ for varying chain length as shown in Fig. 4(b). The surface tension decreases exponentially when N_c increases. In this simulation, we obtained that the surface tension of the droplet is proportional to N_c^{-1}. Figures 4(c) are equilibrium snapshots for $N = 30\,720$. As N_c increases, the droplet surface also becomes rougher. Therefore, it suggests that increased roughness in the droplet surface is indicative of higher capillary wave activity.

The droplet radius increases with increasing chain length. The reason is that the equilibrium bond length is greater than a nonbonded distance [see Fig. 5(a)]. Note that this general

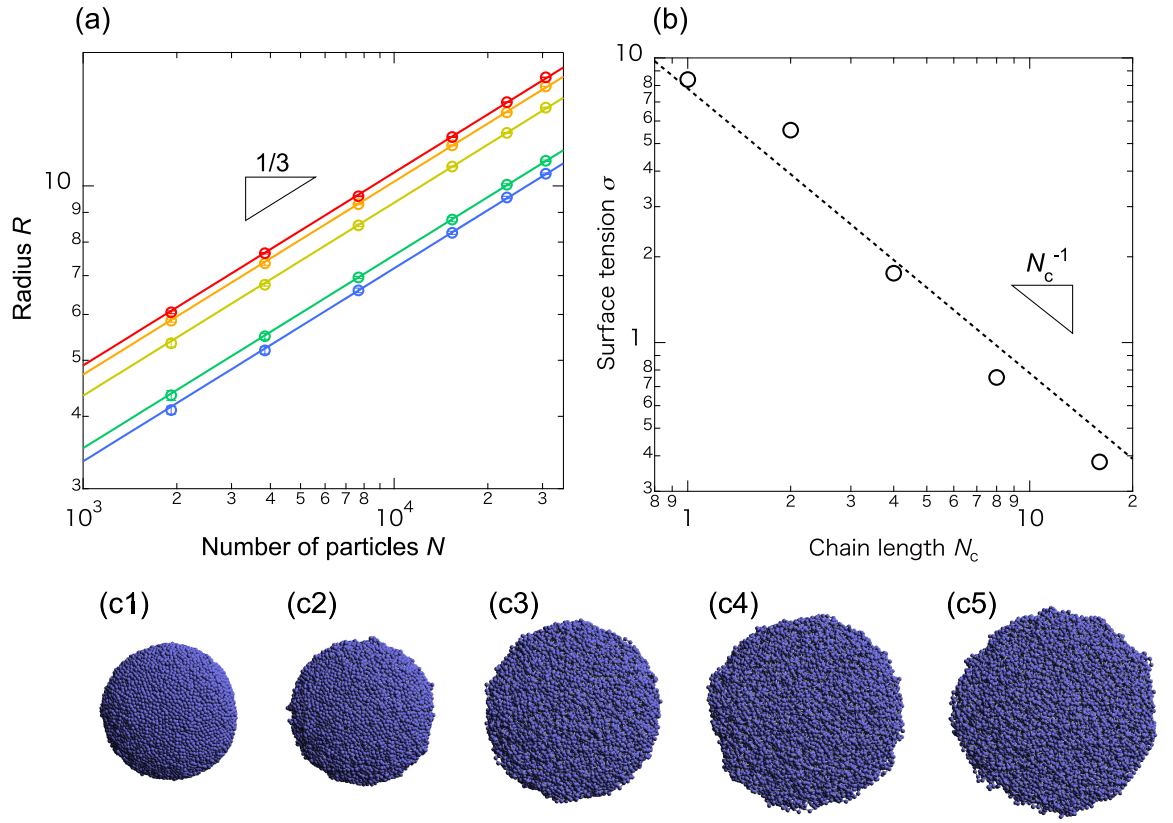

FIG. 4. (a) Relationship between the droplet radius (R) and the number of the particles (N). The solid lines are the fitting results in the form of $R(N) = C \times N^{1/3}$. (b) Equilibrium snapshots for $N = 30\,720$. ($\tau = 5000$) (b1) $N_c = 1$, (b2) $N_c = 2$, (b3) $N_c = 4$, (b4) $N_c = 8$, (b5) $N_c = 16$. (c) Radial distribution functions of (b).

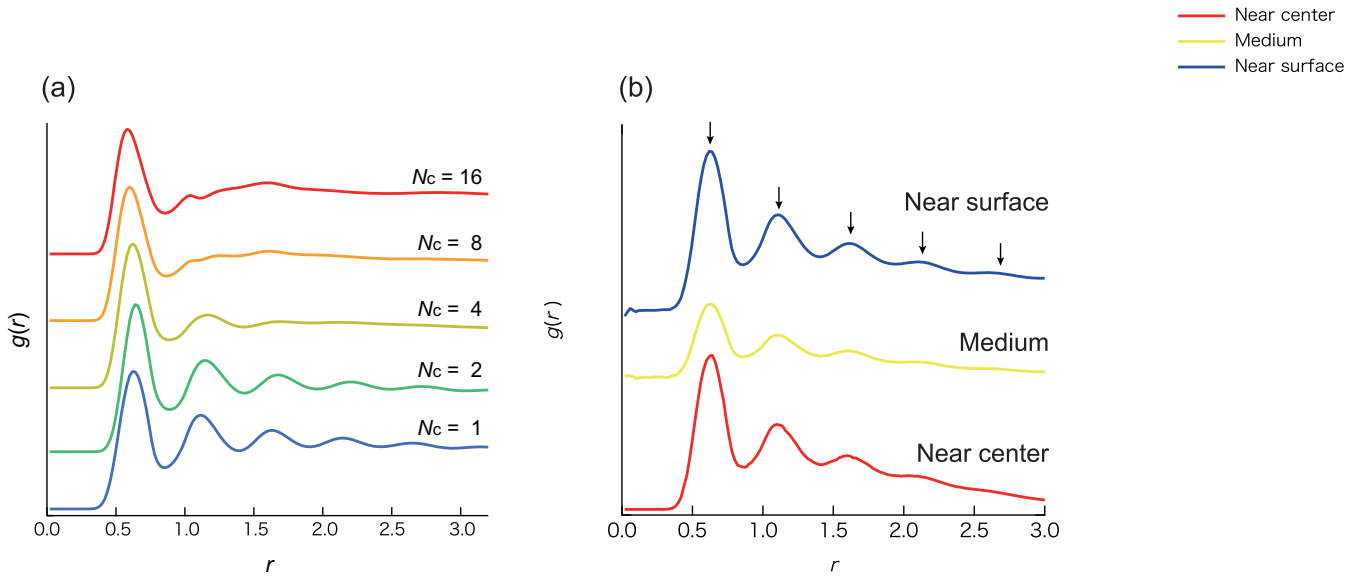

FIG. 5. (a) The radial distribution functions $g(r)$ depending on the chain length and (b) dependence of $g(r)$ on location in the droplet. ($N = 30\,720$ and $N_c = 1$).

relationship is satisfied in many coarse-grained molecular simulation studies. For example, the Kremer-Grest model [45,46], a typical model for coarse-grained MD simulation, satisfies this relationship. Even though R only changes slightly between $N_c = 1$ and 2, it increases significantly when $N_c = 4$. Moreover, subsequent doublings of the chain length produce increasingly diminishing differences. Thus, the dependence of R on N_c is expected to be an effect of a small molecule.

In order to clarify the reason for this, we calculated the radial distribution function (RDF) as shown in Fig. 4(c). For all N_c values, the sharp first peak of RDF arises at $r \sim 0.6$ (Note: it is smaller than the equilibrium bond length). However, the second and third peaks are quite different between $N_c \leqslant 2$ and $N_c \geqslant 4$. The RDF is similar to that of a monoatomic molecule (e.g., Argon) in the liquid phase. In this simulation, five distinct peaks are observed for the r range from 0.0 to 3.2. Meanwhile, when $N_c \geqslant 4$, the second and subsequent peaks are not distinct. It suggests that long-order structures ($r > 1.5$) are hardly formed as the chain length increases. A gap is formed between the chains. Hence, the radius of the droplet increases for longer chain length.

We also calculated the $g(r)$ depending on the location in the droplet as shown in Fig. 5(b). The $g(r)$ near the center region shows a sharp peak and then decays relatively rapidly for $r > 2.0$. In the medium region, a first peak is narrow compared with other locations. The $g(r)$ near the surface shows some sharp peaks, in other words, it decays most slowly. The result suggests the ordering more pronounced near the free surface of the droplet. This trend was observed in all sizes of droplets in our simulation.

Moreover, the size of the droplet may be affected by the radius of gyration (Rg), which is a function of N_c and

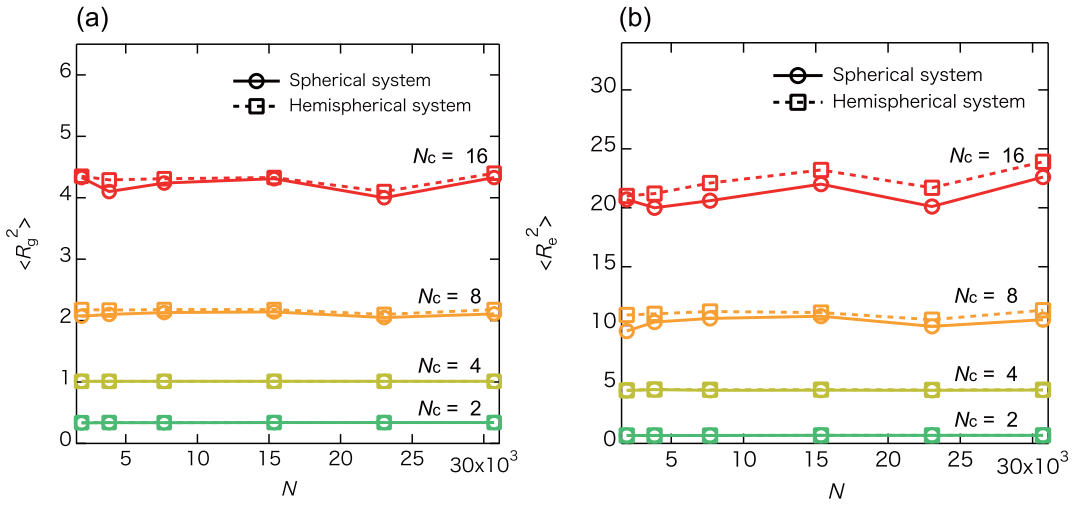

FIG. 6. Number of particles dependence of (a) the mean-square radius of gyration $\langle R_g \rangle$ and (b) the mean-square end-to-end distance $\langle R_e \rangle$. Circles and squares represent spherical and hemispherical droplet system, respectively.

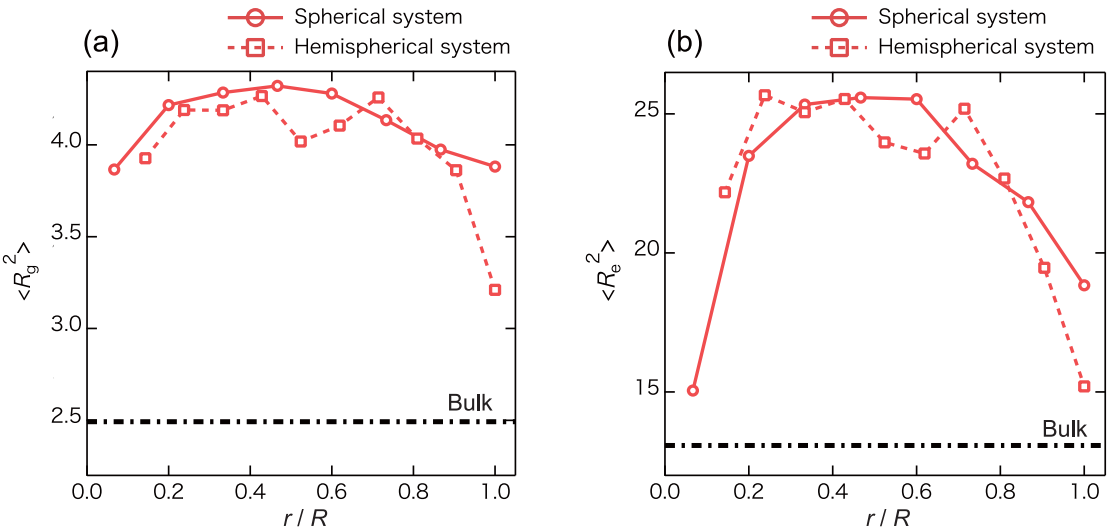

FIG. 7. Dependencies of (a) the mean-square radius of gyration $\langle R_g \rangle$ and (b) the mean-square end-to-end distance $\langle R_e \rangle$ on location in the droplet ($N = 30\,240$ and $N_c = 16$). Circles and squares represent spherical and hemispherical droplet system, respectively. The $\langle R_g \rangle$ and the $\langle R_e \rangle$ of bulk system are represented by dashed-dotted line.

included in the constant C in Eq. (6). It is further discussed in the next section.

C. End-to-end distance and radius of gyration

In order to investigate the effect of the system size on polymer length, we computed the mean square of the radius of gyration $\langle R_g^2 \rangle$ and the mean square end-to-end distance $\langle R_e^2 \rangle$. The radius of gyration and the square end-to-end distance are defined by

$$R_g^2 = \frac{1}{N_c} \sum_i |\boldsymbol{r}_i - \boldsymbol{r}_g|^2 \tag{7}$$

and

$$R_e^2 = |\boldsymbol{r}_1 - \boldsymbol{r}_{N_c}|^2, \tag{8}$$

respectively. Here, $\boldsymbol{r}_g$ is a center of mass of a polymer chain. As shown in Fig. 6, $\langle R_g^2 \rangle$ is nearly the same across all N values for each given N_c, and it changes little between the free spherical droplet and the hemispherical one on the solid wall. $\langle R_e^2 \rangle$ also seems to be independent of N. On the other hand, the hemispherical droplet has slightly larger $\langle R_e^2 \rangle$ than the spherical droplet when $N_c \geqslant 8$. In conclusion, the behavior of the polymer is not much affected by the system size.

For the freely jointed chain, $\langle R_e^2 \rangle = 6\langle R_g^2 \rangle$. In our simulation, $\langle R_e^2 \rangle / \langle R_g^2 \rangle \approx 5$ was obtained due to the lower values of $\langle R_e^2 \rangle$. This result indicates that the polymer cannot spread sufficiently, owing to the vapor-liquid interface.

Next, we investigated dependencies of $\langle R_g \rangle$ and $\langle R_e \rangle$ on location in the droplet as shown in Fig. 7. Both $\langle R_g \rangle$ and $\langle R_e \rangle$ are higher than values on bulk. Thus, we found that each polymer chain is elongated compared with that in bulk (polymer melt), and the stretching effect is weak near the central region and the surface of the droplet. This trend was observed in all Ns.

Finally, we examine the relationship between R_g and the constant C in Eq. (6), as shown in Fig. 8. Since R_g is almost constant for any given N_c [Fig. 6(a)], its value is taken as the ensemble average for each N_c: $R_g = 0.58$, 1.01, 1.46, and 2.06 when $N_c = 2$, 4, 8, and 16, respectively. As a result, $C \propto R_g^{-1}$ is obtained. In other words, we can expect the radius of the droplet to become saturated as N_c increases.

D. Contact angle

In the second series of simulations, we set the DPD particles to form a hemispherical shape on a solid surface, as shown in Fig. 1(b). Then, the contact angle (θ) of the polymer droplet is calculated for different chain lengths and system sizes. To estimate the contact angle between a solid surface and the droplet, we calculated the density distribution in the same manner as for estimating the radius based on prior studies [47–49]. First, the droplet is divided into thin layers in the z direction, as shown in Fig. 9. Then, the density

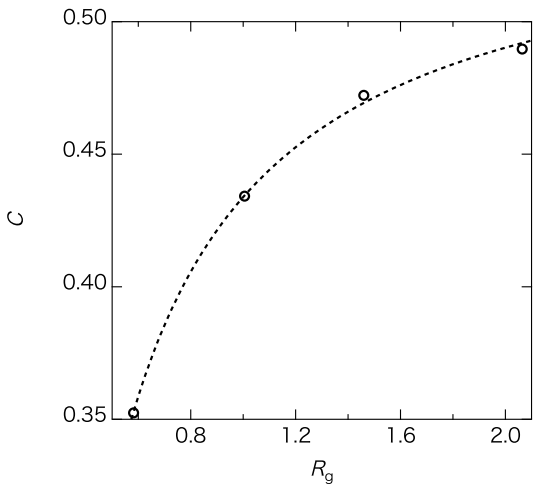

FIG. 8. Relationship between the radius of gyration R_g and the fitting constant C.

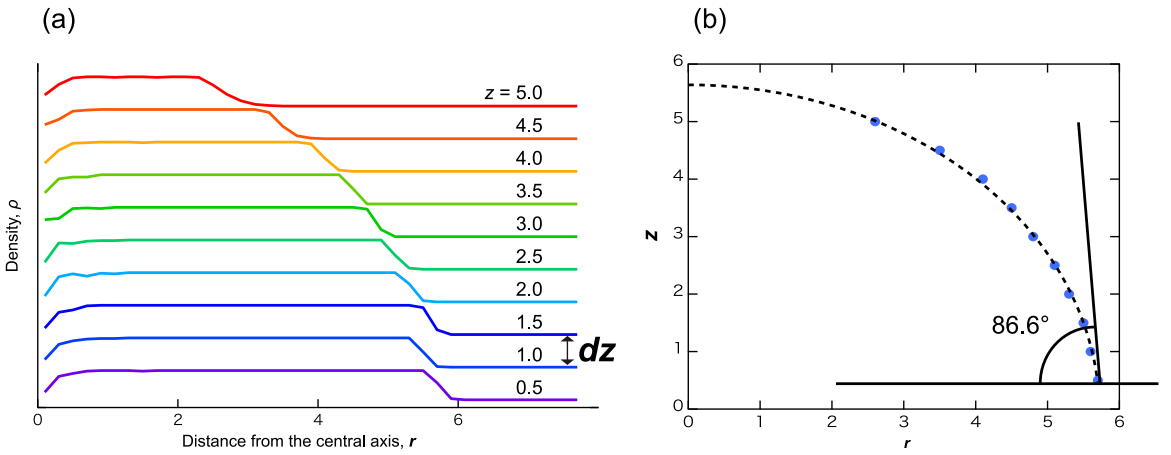

FIG. 9. An outline of the computational procedure of the contact angle between a solid surface and a droplet. The droplet is divided into thin layers in the z direction to calculate a density distribution. Here the distance between adjacent layers (dz) is set to 0.5. (a) The density distributions at $N = 1920$ and $N_c = 1$. We determined a surface position in each layer when ρ drops to half the value at $r = 0$. (b) The contact angle is computed from the angle between the circle and the solid surface at their intersection.

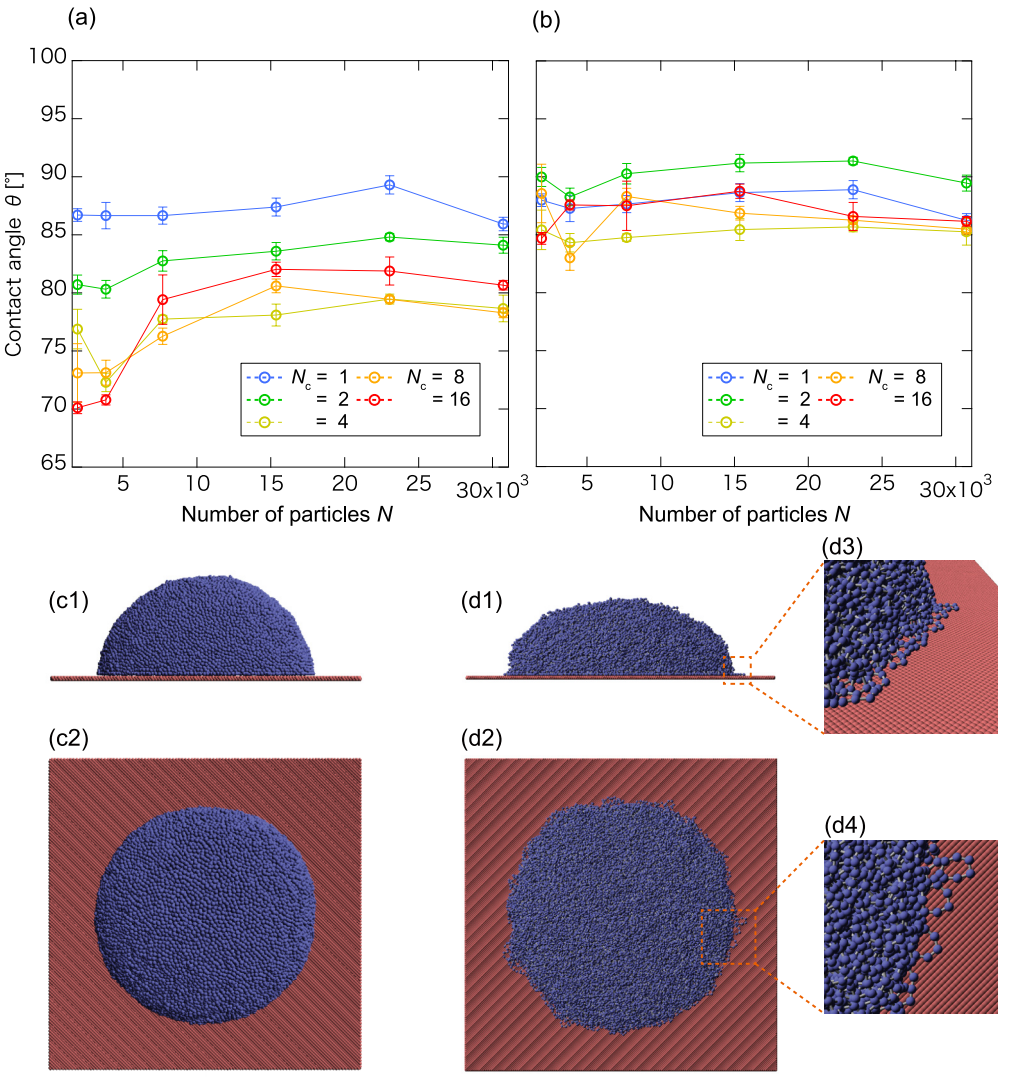

FIG. 10. (a) Relationship between the contact angle (θ) and the number of the particles (N). (b) Relationship between θ and N after a correction. (c, d) Equilibrium snapshots for droplet on the solid surface for $N = 30\,720$. ($\tau = 5000$) (c) $N_c = 1$ of view in the x-z plane (c1) and in the x-y plane (c2). (d) $N_c = 8$ of view in the x-z plane (d1) and in the x-y plane (d2). (d3) and (d4) are enlarged figures of (d1) and (d2), respectively.

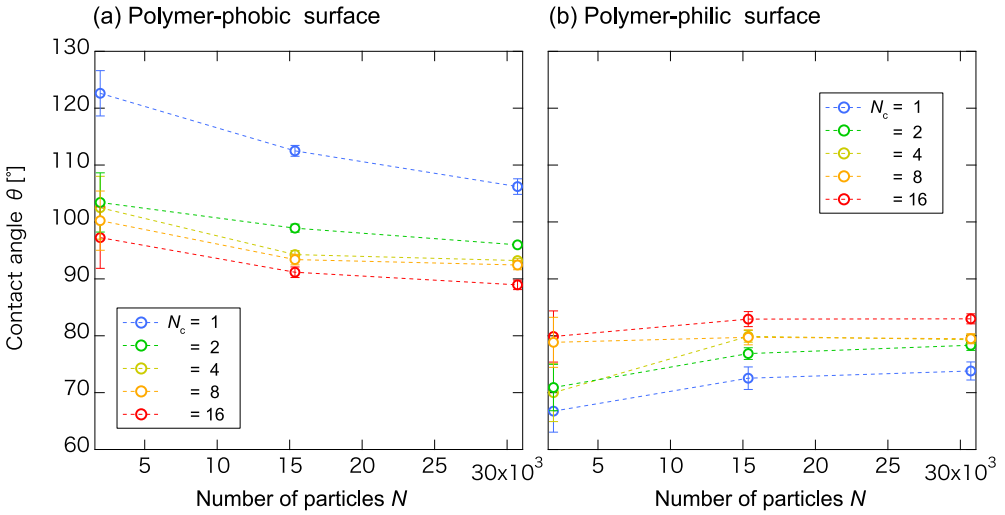

FIG. 11. Relationship between the correction contact angle and the number of the particles when two types of an affinity with the solid surface such as a polymerphobic surface (a) and polymerphilic surface (b). Interaction parameters a_{PS} in polymerphobic and polymerphilic surfaces were set at $-15\ k_BT$ and $-35\ k_BT$, respectively.

distribution is obtained by computing the density in each layer at different distances from the central axis. The distance between adjacent layers, dz, is set to 0.5. Figure 9(a) shows the density distributions at $N = 1920$ and $N_c = 1$. The vertical axis is the density ρ, and the horizontal axis, r, is the distance from the central axis of the droplet. Similar to the definition of R in Sec. III A, we determined a surface position in each layer when ρ drops to half the value at $r = 0$. These positions in each layer are fitted to a circle as shown in Fig. 9(b). θ is computed from the angle between the circle and the solid surface at their intersection. When $N = 1920$ and $N_c = 1$, θ is about 86.6°.

Using the method, we computed 30 contact angles for different conditions, and summarized them in Fig. 10(a). First, we noticed that the value of θ fluctuates as the chain length N increases. When $N_c = 1$, the contact angle is almost constant (∼84°) for all values of N. On the other hand, as N_c increases beyond 4, smaller droplets ($N < 10\,000$) have lower θ than larger droplets. This means that the size of the system has a strong effect on the contact angle, particularly when N_c is large. Therefore, a large number of particles ($N > 15\,000$) are needed when simulating the contact angle of droplets, so as not to underestimate it (i.e., more polymerphilic) for longer chain lengths.

Next, we found that the contact angle depends on the chain length. At the highest N value, θ is about 88° when $N_c = 1$, and only about 80° at $N_c = 16$. The dumbbell-shaped molecules ($N_c = 2$) have an intermediate contact angle ($\theta \sim 84°$). If N is sufficiently large, θ is almost constant when $N_c \geqslant 4$. These results indicate that a droplet composed of a monoatomic molecule has less affinity with the solid surface compared with that of polymer molecule with the same number of monomers.

Generally, the bulk domain in a droplet is more stable energetically compared to the interface domain. Hence, molecules on the droplet surface fluctuate significantly, especially when N_c is large [Figs. 10(c) and 10(d)]. Polymers near a solid surface contact [Figs. 10(d3) and 10(d4)] spread onto the surface via the formation of a precursor foot [17] to reduce the surface energy, as the solid-liquid surface is lower in energy than the vapor-liquid one. Taking this into account, we corrected the contact angle by fitting using points except for the distance in the interaction from the solid wall. In Fig. 10(b), the contact angles for $N_c = 1$ remain almost unchanged after the correction, whereas the others increase to values similar to when $N_c = 1 (85° < \theta < 90°)$. Such significant changes imply that the polymerphilic behavior in a polymer droplet is governed by the polymer molecules in the vicinity of the surface.

Finally, we also compared the correction contact angle when the surface is polymerphobic, polymerphilic, or polymer-neutral, in order to evaluate the effect of wettability. The results are summarized in Fig. 11. Similar to the neutral case, the contact angles on the other two surfaces also depend on the polymer chain length N_c. As N_c increases, θ decreases for the polymerphobic surface, on which the contact angles at $N_c = 1$, 2, 4, 8, and 16 are 108°, 97°, 93°, 92°, and 89°, respectively [Fig. 11(a)]. In contrast, as N_c increases, θ increases for the polymerphilic surface. The contact angles in $N_c = 1$, 2, 4, 8, and 16 are calculated as 74°, 78°, 79°, 79°, and 81°, respectively [Fig. 11(b)]. Altogether, the effect of the affinity with the solid surface increases when the chain length of the polymer increases.

On the polymerphilic surface, the contact angle increases (i.e., the wettability decreases) as the chain length increases. This result is consistent with early studies [17,19] of such spreading. As N_c increases beyond a critical value, the spreading is inhibited by molecular entanglement. In contrast, polymers near the polymerphobic solid surface come into contact with the surface and spread on it via the formation of a precursor foot to reduce the surface energy. Consequently, the contact angle decreases as N_c increases, implying increased affinity between the droplet and surface. Hence, we found that there is a critical affinity for the monomer on the solid surface; above and below which the wettability increases and decreases as the molecular length increases, respectively. However, a

contact angle is not reversed between polymerphobic and polymerphilic walls, but it is expected to asymptotically approach a certain value.

IV. CONCLUSION

In conclusion, we performed MDPD simulation for the spherical droplet in vacuum and hemispherical droplet on solid surfaces, in order to investigate the effects of the chain length of the polymer (N_c) and the total number of particles (N) on the static behavior of the droplet, namely the radius and the contact angle.

First, we described the validation of the MDPD method with the entanglement force by confirming the droplet behaviors satisfy the Laplace law. As a result, the pressure difference increased in proportion to $1/R$. The simulation method satisfies the Laplace law; therefore, the validity of the simulation method was proved.

For the spherical droplet with a given N value, the radius of the droplet increased with N_c. For a given N_c value, this radius was proportional to $N^{1/3}$. Since the latter scaling relationship indicates a weak dependency on N, the size and shape of a polymer droplet can be predicted by simulating a smaller system ($N < 2000$).

We also calculated the radial distribution function $g(r)$ depending on the location in the droplet. The $g(r)$ near the center region decayed relatively rapidly, meanwhile that near the surface decayed most slowly. The result suggests the ordering more pronounced near the free surface of the droplet. Additionally, we investigated dependencies of the mean square of the radius of gyration $\langle R_g \rangle$ and the mean-square end-to-end distance $\langle R_e \rangle$ on location in the droplet. Both $\langle R_g \rangle$ and $\langle R_e \rangle$ were higher than values in bulk. Thus, we found that each polymer chain is elongated compared with that in bulk (polymer melt), and the stretching effect is weak near the central region and the surface of the droplet.

For the hemispherical droplet on the solid surface, the simulated contact angle (θ) for a comparatively small droplet ($N < 10\,000$) was lower than that for a large droplet. This means that the size of the system has a comparatively stronger effect on the contact angle. This trend was particularly conspicuous when N_c is large. These results suggest that a large number of particles ($N > 15\,000$) have to be included to calculate the proper contact angle, otherwise this angle will be underestimated (more polymerphilic), especially when the chain length is long. We also studied the effect of wettability of the solid surface by using polymerphobic and polymerphilic surfaces. As N_c increases, θ decreases on the polymerphobic surface and increased on the polymerphilic one. We found that there is a critical affinity for the monomer on the solid surface; above and below which the wettability increased and decreased as the molecular length increased, respectively.

[1] P. Day, A. Manz, and Y. Zhang, *Microdroplet Technology: Principles and Emerging Applications in Biology and Chemistry* (Springer-Verlag, New York, 2012).

[2] W. Barthlott and C. Neinhuis, Purity of the sacred lotus, or escape from contamination in biological surfaces, Planta **202**, 1 (1997).

[3] Y. Ding, S. Xu, Y. Zhang, A. C. Wang, M. H. Wang, Y. Xiu, C. P. Wong, and Z. L. Wang, Modifying the anti-wetting property of butterfly wings and water strider legs by atomic layer deposition coating: Surface materials versus geometry, Nanotechnology **19**, 355708 (2008).

[4] Y. Su, B. Ji, Y. Huang, and K. Hwang, Natures design of hierarchical superhydrophobic surfaces of a water strider for low adhesion and low-energy dissipation, Langmuir **26**, 18926 (2010).

[5] E. Mele, S. Girardo, and D. Pisignano, Strelitzia reginae leaf as a natural template for anisotropic wetting and superhydrophobicity, Langmuir **28**, 5312 (2012).

[6] H. K. Webb, R. J. Crawford, and E. P. Ivanova, Wettability of natural superhydrophobic surfaces, Adv. Colloid Interface Sci. **210**, 58 (2014).

[7] H. Sirringhaus, T. Kawase, R. H. Friend, T. Shimoda, M. Inbasekaran, W. Wu, and E. P. Woo, High-resolution inkjet printing of all-polymer transistor circuits, Science **290**, 2123 (2000).

[8] K. Arai, S. Iwanaga, H. Toda, C. Genci, Y. Nishiyama, and M. Nakamura, Three-dimensional inkjet biofabrication based on designed images, Biofabrication **3**, 034113 (2011).

[9] C. J. Ferris, K. G. Gilmore, G. G. Wallace, and M. in het Panhuis, Biofabrication: An overview of the approaches used for printing of living cells, Appl. Microbiol. Biotechnol. **97**, 4243 (2013).

[10] J. Z. Wang, Z. H. Zheng, H. W. Li, W. T. S. Huck, and H. Sirringhaus, Dewetting of conducting polymer inkjet droplets on patterned surfaces, Nat. Mater. **3**, 171176 (2004).

[11] F. Léonforte and M. Müller, Statics of polymer droplets on deformable surfaces, J. Chem. Phys. **135**, 214703 (2011).

[12] J. Perelaer, P. J. Smith, E. van den Bosch, S. S. C. van Grootel, P. H. J. M. Ketelaars, and U. S. Schubert, The spreading of inkjet-printed droplets with varying polymer molar mass on a dry solid substrate, Macromol. Chem. Phys. **210**, 495 (2009).

[13] P. E. Rouse, A theory of the linear viscoelastic properties of dilute solutions of coiling polymers, J. Chem. Phys. **21**, 1272 (1953).

[14] M. Doi and S. F. Edwards, *The Theory of Polymer Dynamics* (Clarendon, Oxford, 1986).

[15] P. G. de Gennes, Reptation of a polymer chain in the presence of fixed obstacles, J. Chem. Phys. **55**, 572 (1971).

[16] M. Doi and S. F. Edwards, Dynamics of concentrated polymer systems. Part 1. Brownian motion in the equilibrium state, J. Chem. Soc., Faraday Trans. 2 **74**, 1789 (1978).

[17] D. R. Heine, G. S. Grest, and E. B. Webb III, Spreading dynamics of polymer nanodroplets, Phys. Rev. E **68**, 061603 (2003).

[18] D. R. Heine, G. S. Grest, and E. B. Webb III, Surface Wetting of Liquid Nanodroplets: Droplet-Size Effects, Phys. Rev. Lett. **95**, 107801 (2005).

[19] B. Noble, A. Ovcharenko, and B. Raeymaekers, Quantifying lubricant droplet spreading on a flat substrate using molecular dynamics, Appl. Phys. Lett. **105**, 151601 (2014).

[20] J. H. Maas, M. A. Cohen Stuart, F. A. M. Leermakers, and N. A. M. Besseling, Wetting transition in a polymer brush: Polymer droplet coexisting with two film thicknesses, Langmuir **16**, 3478 (2000).
[21] A. Milchev and K. Binder, Polymer melt droplets adsorbed on a solid wall: A Monte Carlo simulation, J. Chem. Phys. **114**, 8610 (2000).
[22] I. Pagonabarraga and D. Frenkel, Dissipative particle dynamics for interacting systems, J. Chem. Phys. **115**, 5015 (2001).
[23] S. Trofimov, E. Nies, and M. Michels, Thermodynamic consistency in dissipative particle dynamics simulations of strongly nonideal liquids and liquid mixtures, J. Chem. Phys. **117**, 9383 (2002).
[24] P. B. Warren, Vapor-liquid coexistence in many-body dissipative particle dynamics, Phys. Rev. E **68**, 066702 (2003).
[25] S. Trofimov, E. Nies, and M. Michels, Constant-pressure simulations with dissipative particle dynamics, J. Chem. Phys. **123**, 144102 (2005).
[26] P. Hoogerbrugge and J. Koelman, Simulating microscopic hydrodynamic phenomena with dissipative particle dynamics, Europhys. Lett. **19**, 155 (1992).
[27] P. Espanõl and P. Warren, Statistical mechanics of dissipative particle dynamics, Europhys. Lett. **30**, 191 (1995).
[28] R. Groot and P. Warren, Dissipative particle dynamics: Bridging the gap between atomistic and mesoscopic simulation, J. Chem. Phys. **107**, 4423 (1997).
[29] T. Kinjo and S. Hyodo, Linkage between atomistic and mesoscale coarse-grained simulation, Mol. Simul. **33**, 417 (2007).
[30] T. Kinjo and S. A. Hyodo, Equation of motion for coarse-grained simulation based on microscopic description, Phys. Rev. E **75**, 051109 (2007).
[31] C. Chen, C. Gao, L. Zhuang, X. Li, P. Wu, J. Dong, and J. Lu, A many-body dissipative particle dynamics study of spontaneous capillary imbibition and drainage, Langmuir **26**, 9533 (2010).
[32] C. Chen, L. Zhuang, X. Li, J. Dong, and J. Lu, A many-body dissipative particle dynamics study of forced water-oil displacement in capillary, Langmuir **28**, 1330 (2012).
[33] Z. Li, G.-H. Hu, Z.-L. Wang, Y.-B. Ma, and Z.-W. Zhou, Three dimensional flow structures in a moving droplet on substrate: A dissipative particle dynamics study, Phys. Fluids **25**, 072103 (2013).
[34] Y. Wang and S. Chen, Numerical study on droplet Sliding across micropillars, Langmuir **31**, 4673 (2015).
[35] P. B. Warren, Hydrodynamic Bubble Coarsening in Off-Critical Vapor-Liquid Phase Separation, Phys. Rev. Lett. **87**, 225702 (2001).
[36] N. Spenley, Scaling laws for polymers in dissipative particle dynamics, Europhys. Lett. **49**, 534 (2000).
[37] M. Langeloth, Y. Masubuchi, M. C. Böhm, and F. Müller-Plathe, Recovering the reputation dynamics of polymer melts in dissipative particle dynamics simulations via slip-springs, J. Chem. Phys. **138**, 104907 (2013).
[38] T. Sirk, Y. Slizoberg, J. Brennan, M. Lisal, and J. Andzelm, An enhanced entangled polymer model for dissipative particle dynamics, J. Chem. Phys. **136**, 134903 (2012).
[39] S. Yamamoto and S. Hyodo, A Computer simulation study on the mesoscopic structure of the polyelectrolyte membrane Nafion, Polym. J. **35**, 519 (2003).
[40] M. Deng, Y. Jiang, X. Li, L. Wang, and H. Liang, Conformational behaviors of a charged-neutral star micelle in salt-free solution, Phys. Chem. Chem. Phys. **12**, 6135 (2010).
[41] N. Arai, K. Yasuoka, and X. C. Zeng, A vesicle cell under collision with a Janus or homogeneous nanoparticle: Translocation dynamics and late-stage morphology, Nanoscale **5**, 9089 (2013).
[42] M. Arienti, W. Pan, X. Li, and G. Karniadakis, Many-body dissipative particle dynamics simulation of liquid/vapor and liquid/solid interactions, J. Chem. Phys. **134**, 204114 (2011).
[43] C. Chen, K. Lu, X. Li, J. Dong, J. Lu, and L. Zhuang, A many-body dissipative particle dynamics study of fluid-fluid spontaneous capillary displacement, RSC Adv. **4**, 6545 (2014).
[44] A. Tiwari and J. Abraham, Dissipative-particle-dynamics model for two-phase flows, Phys. Rev. E **74**, 056701 (2006).
[45] K. Kremer and G. S. Grest, Dynamics of entangled linear polymer melts: A moleculardynamics simulation, J. Chem. Phys. **92**, 5057 (1990).
[46] K. Kremer and G. S. Grest, Molecular dynamics (MD) simulations for polymers, J. Phys. Condens. Matter **2**, SA295 (1990).
[47] M. J. de Ruijter, T. D. Blake, and J. De Coninck, Dynamic wetting studied by molecular modeling simulations of droplet spreading, Langmuir **15**, 7836 (1999).
[48] T. Ingebrigtsen and S. Toxvaerd, Contact angles of Lennard-Jones liquids and droplets on planar surfaces, J. Phys. Chem. **111**, 8518 (2007).
[49] B. Shi and V. K. Dhir, Molecular dynamics simulation of the contact angle of liquids on solid surfaces, J. Chem. Phys. **130**, 034705 (2009).